

Vibrational Fingerprints of Strained Polymers: A Spectroscopic Pathway to Mechanical State Prediction

Julian Konrad^{*a}, Janina Mittelhaus^b, David M. Wilkins^c, Bodo Fiedler^b, and Robert Meißner^{a,d}

^aHamburg University of Technology, Institute for Interface Physics and Engineering, Am Irrgarten 3–9, 21073 Hamburg, Germany

^bHamburg University of Technology, Institute of Polymers and Composites, Denickestraße 15, 21073 Hamburg, Germany

^cCentre for Quantum Materials and Technologies, School of Mathematics and Physics, Queen’s University Belfast, Belfast BT7 1NN, Northern Ireland, United Kingdom

^dHelmholtz-Zentrum Hereon, Institute of Surface Science, Max-Planck-Straße 1, 21502 Geesthacht, Germany

Abstract

The vibrational response of polymer networks under load provides a sensitive probe of molecular deformation and a route to non-destructive diagnostics. Here we show that machine-learned force fields reproduce these spectroscopic fingerprints with quantum-level fidelity in realistic epoxy thermosets. Using MACE-OFF23 molecular dynamics, we capture the experimentally observed redshifts of *para*-phenylene stretching modes under tensile load, in contrast to the harmonic OPLS-AA model. These shifts correlate with molecular elongation and alignment, consistent with Badger’s rule, directly linking vibrational features to local stress. To capture IR intensities, we trained a symmetry-adapted dipole moment model on representative epoxy fragments, enabling validation of strain responses. Together, these approaches provide chemically accurate and computationally accessible predictions of strain-dependent vibrational spectra. Our results establish vibrational fin-

*Email: julian.konrad@tuhh.de

gerprints as predictive markers of mechanical state in polymer networks, pointing to new strategies for stress mapping and structural-health diagnostics in advanced materials.

Introduction

Non-destructive diagnostics of mechanical deformation in polymeric materials are a central challenge in the design of high-performance composites and structural systems [1]. While macroscopic properties such as stiffness and toughness are routinely evaluated, molecular signatures of stress and strain remain difficult to access. Vibrational spectroscopy provides a direct pathway, revealing local structural changes through frequency shifts. Because many structural composites rely on crosslinked polymer networks, particularly epoxy resins, for strength, chemical resistance, and thermal stability [2, 3], it is crucial to understand how mechanical load imprints on their spectroscopic features. Yet this connection remains poorly resolved.

In confined microscale domains, such as thin films between fiber layers, epoxy networks show deformation behaviors that diverge from bulk properties, including unexpected ductility under tension [4, 5, 6, 7, 8, 9]. These findings underscore the role of network topology and nanoscale dynamics in governing mechanical and vibrational response.

To probe these effects, molecular dynamics (MD) simulations have been widely used to investigate the atomic-scale response of crosslinked epoxy networks under load [10, 11, 12, 13, 14, 9]. While their mechanical performance has been extensively modeled, strain-dependent vibrational behavior – especially in confined environments [15] – remains far less explored.

This gap is partly due to the limitations of current computational approaches for modeling vibrational spectra. Quantum chemical methods such as density functional theory yield accurate vibrational frequencies for isolated molecules [16, 17], and have been used to characterize thermoset monomers in the gas phase [18, 8]. However, they do not capture the influence of the surrounding network. Density-functional perturbation theory extends this capability to condensed phases [19], but with a computational expense that confines applications to small and idealized systems.

Ab-initio MD offers a more realistic sampling of vibrational dynamics in the condensed phase by incorporating finite-temperature and many-body effects [20, 21, 22], but it remains computationally prohibitive for large crosslinked networks. Classical MD with empirical force fields such as OPLS-AA [23] can access larger systems, but their treatment of bonds as harmonic and their neglect of polarization and charge redistribution [24] limit accuracy for vibrational spectra.

Machine-learned (ML) potentials bridge this gap by reproducing quantum-level accuracy at MD scales. Approaches such as Behler–Parrinello networks, Gaussian approximation potentials, and equivariant message-passing models like NequIP have demonstrated broad success [25, 26, 27, 28, 29, 30]. The MACE-OFF23 force field [31], developed for organic chemistry, captures anharmonicity, topological complexity, and local environmental effects, making it well-suited for polymer systems. ML potentials have recently been applied to diverse condensed-phase systems, ranging from silicates at extreme conditions [32] to thermosets [33], expanding their role in materials science. However, prior studies used alternative ML formalisms, and MACE-OFF23 has not yet been applied to thermosets.

Beyond ML force fields, recent advances in machine-learned models enable prediction of dipole moments and polarizabilities directly from molecular configurations [34, 35, 36, 37, 30, 38]. Such models extend the spectroscopic fidelity of classical and neural-network dynamics by providing IR-intensity information otherwise inaccessible in fixed-charge or non-polarizable potentials. Combining ML force fields such as MACE with symmetry-adapted Gaussian process regression (SAGPR) [39] enables chemically accurate simulations of both vibrational frequencies and intensities in extended polymer networks.

In this paper, we investigate the vibrational properties of crosslinked epoxy networks under uniaxial tension using MD simulations and experimental *in-situ* tensile tests on film samples made from bisphenol A diglycidyl ether (DGEBA) and an aliphatic hardener to verify the simulation results. We analyze redshifts in the *para*-phenylene stretching modes and bending vibrations of aromatic hydrogens under load [40]. For the MD simulations, two epoxy systems, each composed of a different resin monomer and either an aliphatic or an aromatic hardener, are examined with both the classical OPLS-AA force field and the ML potential MACE-OFF23. In addition, we train a machine-learned dipole model

on chemically representative epoxy fragments and apply it to fragment-level simulations to provide IR-intensity information complementary to velocity-based spectra. Together, these approaches bridge the gap between molecular-scale structure and vibrational response under strain in crosslinked polymer networks. By combining charge-weighted VACF analysis, ML potentials, and SAGPR-derived dipoles, we resolve strain-induced modifications to aromatic vibrational signatures. This framework reveals the molecular origins of spectral changes under stress, establishing a foundation for non-destructive diagnostics and reliability assessment in polymer networks.

Methods and Models

To construct the molecular models, we initialized all systems from SMILES representations [41] of the monomers bisphenol F diglycidyl ether (BFDGE), bisphenol A diglycidyl ether (DGEBA), diethyltoluenediamine (DETDA), and diethylenetriamine (DETA). The molecular structures were parameterized with the OPLS-AA force field, assigned via LigParGen [42], and we refined atomic charges using restrained electrostatic potential (RESP) fitting. We simplified molecular topologies with the TEMPLATER tool and generated reduced force fields and reaction templates following Konrad and Meißner [43].

We used LAMMPS [44] to model the crosslinking reactions and bulk polymer formation of the BFDGE-DETDA and DGEBA-DETA epoxy networks. Each simulation box contained 160 resin molecules (BFDGE or DGEBA) and 80 DETDA or 64 DETA hardener molecules, yielding total system sizes of 9360 (BFDGE-DETDA) and 9120 (DGEBA-DETA) atoms. We equilibrated the systems in the NPT ensemble for 2 ns, followed by a crosslinking procedure performed over 2 ns at 600 K using the LAMMPS REACTION package [45]. In case of a reaction happening, we used a time step of 0.5 fs, and applied the NVE/limit integrator for 500 fs to constrain reactive-site displacements to 0.0015 Å per fs.

We applied Nosé–Hoover thermostat and barostat coupling with damping constants of 100 fs and 1000 fs, respectively, at a pressure of 1 atm [46]. Periodic boundary conditions were imposed in all directions. We computed Lennard-Jones interactions with an 8 Å cutoff

and short-range electrostatics with a 12 Å cutoff. Long-range electrostatics were treated using the particle–particle particle–mesh method with a (relative) k -space accuracy of 1.0×10^{-4} [47].

Following the crosslinking process, we equilibrated each cured epoxy network for 2 ns at 300 K to allow structural relaxation. We computed elastic moduli via linear response theory based on equilibrium trajectory sampling under a triclinic barostat over a 10 ns interval, in accordance with prior studies [12, 13]. To assess the mechanical response, we applied uniaxial tensile deformation up to a total strain of 0.5 %, using a constant strain rate of $\dot{\epsilon} = 5 \cdot 10^7 \text{ s}^{-1}$. To reduce potential strain-rate artifacts, we conducted additional constant-strain relaxation simulations at intermediate strain levels of 0.03, 0.05, 0.125, 0.25, 0.375, and 0.5, each maintained for 5 ns.

To analyze the vibrational properties, we recorded atomic velocities from equilibrated structures over 50 ps with a 0.25 fs time step, employing both the classical OPLS-AA force field [23] and the ML potential MACE-OFF23 (small) [48], which captures anharmonic effects through its quantum-mechanical training data. The vibrational power spectra $S(\omega)$ were obtained from the velocity autocorrelation function (VACF) using the Wiener–Khinchin theorem. The VACF was computed as:

$$C_{\mathbf{v} \cdot \mathbf{v}}(\tau) = \frac{1}{N} \sum_{i=1}^N \langle \mathbf{v}_i(t) \cdot \mathbf{v}_i(t + \tau) \rangle, \quad (1)$$

and its Fourier transform yielded the vibrational spectrum:

$$S(\omega) = \int_0^\infty C_{\mathbf{v} \cdot \mathbf{v}}(\tau) e^{-i\omega\tau} d\tau, \quad (2)$$

While IR spectra are conventionally derived from dipole autocorrelations, fixed-charge classical force fields do not account for dynamic charge redistribution. The total dipole moment for systems with fixed atomic charges q_i is given by:

$$\boldsymbol{\mu}(t) = \sum_{i=1}^N q_i \mathbf{r}_i(t), \quad (3)$$

where $\mathbf{r}_i(t)$ is the position of atom i at time t . While this definition is valid for the total system dipole, it does not capture time-dependent polarization or charge transfer effects at the molecular level. To qualitatively account for the influence of partial charges on vibrational dynamics, we employed a charge-weighted velocity autocorrelation function:

$$C_{JJ}(\tau) = \frac{1}{N} \sum_{i=1}^N q_i \langle \mathbf{v}_i(t) \cdot \mathbf{v}_i(t + \tau) \rangle. \quad (4)$$

This approach heuristically emphasizes the motion of atoms with larger partial charges, which are typically located in polar functional groups. These atoms experience stronger local electric field fluctuations during molecular vibrations and thus tend to contribute more prominently to time-dependent dipole fluctuations. Although dynamic polarization is not explicitly modeled, $C_{JJ}(\tau)$ provides a computationally efficient and physically motivated way to improve the interpretability of vibrational spectra from fixed-charge MD simulations.

Starting from the monomeric structures of epoxy precursor moieties (Figure 1), we built simulation systems large enough to capture bulk polymer behavior, while remaining within the computational limits of neural network potentials and the data needs of VACF-based vibrational analysis. Each system contained about 10,000 atoms, with three velocity components per atom, sampled over 200,000 time steps (spanning 50 ps with a 0.25 fs interval). To achieve high wavenumber resolution, we evaluated the autocorrelation over the full lag range of 50 ps. The resulting memory and compute demands necessitated parallel implementation on GPU architectures, and all analyses were performed on NVIDIA A100 and H100 units equipped with 80 GB of RAM. All spectra were broadened using Gaussian convolution with a width σ of 5 cm^{-1} to facilitate peak identification and improve comparability.

To generate a representative training dataset for machine learning-based dipole prediction, we systematically sampled chemically relevant substructures of the epoxy systems. The selected units comprised monomeric BFDGE and DETDA, as well as progressively crosslinked fragments: (i) a single BFDGE covalently linked to DETDA, (ii) two BFDGE molecules doubly connected to a single DETDA, and (iii) a BFDGE unit bridging two

DETDA molecules. These fragments capture the key chemical environments of the bulk networks and provide transferable descriptors for ML dipole models.

We generated conformational ensembles of each fragment using replica exchange molecular dynamics (REMD) with the OPLS-AA force field. Temperature windows spanned 300–580 K in 40 K increments, ensuring coverage of the relevant configurational space. Each REMD trajectory ran for 500 ns, providing sufficient sampling of both local torsional motions and large-scale rearrangements. We extracted structures for QM calculations exclusively from the 300 K replica to retain thermally accessible conformers at ambient conditions. To reduce redundancy, we applied farthest-point sampling in the space of 17 dihedral descriptors, which reflect the dominant internal degrees of freedom of the fragments. This yielded 5000 unique structures per fragment, producing a diverse and balanced dataset.

All QM reference calculations were performed with ORCA 6.1.1 [49] package at the B3LYP/def2-TZVP level of theory. For each structure, we extracted atomic charges, atomic dipole moments, and total molecular dipole vectors.

The molecular dipole moments μ served as training data for a symmetry-adapted Gaussian process regression (SAGPR) model [39, 50]. SAGPR extends standard Gaussian process regression (GPR) to learn properties that transform covariantly under rigid-body rotations. For a molecule \mathcal{M} , the Cartesian components of the predicted dipole moment $\mu(\mathcal{M})$ are given by,

$$\mu_i(\mathcal{M}) = \sum_{m,j} K_{ij}(\mathcal{M}, \mathcal{M}_m) w_{mj}, \quad (5)$$

where the m index runs over all members of an active set as in GPR [51] and $\mathbf{K}(\mathcal{M}, \mathcal{M}')$ is a matrix-valued kernel between two molecules \mathcal{M} and \mathcal{M}' , encoding both the similarity of these two molecules and the symmetry of the problem. When the molecular coordinates are rotated by a given matrix \mathbf{R} , the kernel matrix is transformed as,

$$K_{ij}(\mathbf{R}\mathcal{M}, \mathbf{R}'\mathcal{M}') = \sum_{kl} R_{ik} R'_{jl} K_{kl}(\mathcal{M}, \mathcal{M}'), \quad (6)$$

ensuring that the prediction transforms in the correct way under a rotation. We trained a single SAGPR model on 80% of the molecular fragment dataset. This model, referred

to as μ -EPOXY, is described in detail in the Supplementary Information (Section S2), including the chosen hyperparameters and usage instructions.

To evaluate the performance of the trained SAGPR model in vibrational spectroscopy, we selected a DETDA–BFDGE–DETDA (DBD) fragment as a representative epoxy subunit. This configuration captures the key chemical motifs of the crosslinked networks and served as a benchmark for spectroscopic analysis under molecular strain. Molecular dynamics simulations were carried out with the MACE-OFF23 (small) ML potential [48]. To probe the vibrational response under finite deformation, we applied ten increments of fixed molecular elongation, systematically straining the DBD fragment. At each elongation step, trajectories were propagated for 50 ps with a 0.25 fs time step.

The vibrational spectra were derived via the standard autocorrelation–Fourier transform workflow. Specifically, we computed velocity autocorrelation functions (Equation 4) from the velocity trajectories and Fourier transformed them to obtain vibrational power spectra. In addition, the same trajectories were used to generate instantaneous atomic dipoles from the SAGPR model. From these, we computed a dipole autocorrelation function (Dacf),

$$C_{\mu \cdot \mu}(\tau) = \frac{1}{N} \sum_{i=1}^N \langle \boldsymbol{\mu}_i(t) \cdot \boldsymbol{\mu}_i(t + \tau) \rangle, \quad (7)$$

where $\boldsymbol{\mu}_i(t)$ denotes the instantaneous dipole contribution of atom i . Fourier transformation of the Dacf, followed by multiplication with ω^2 , yielded the corresponding IR spectrum.

The experimental setup combined tensile testing with *in-situ* infrared spectroscopy. We prepared epoxy thin films (30 μm thick) using an infusion process described in detail elsewhere [8, 9]. The resin system consisted of EPIKOTETM Resin MGS RIMR 135 (diglycidyl ether of bisphenol A, DGEBA) and EPIKURETM Curing Agent MGS RIMH 137 (aliphatic diamine hardener), mixed at a 100:30 weight ratio. We punched the films into dogbone specimens (for details on the sample geometry, see [9]) and conducted uniaxial tensile tests at room temperature on a Deben *MT200* microtensile stage with a 20 N load cell, applying a crosshead speed of 1.0 mm min^{-1} . For *in-situ* infrared measurements, we

integrated the tensile stage into a Bruker TENSOR II spectrometer. We collected spectra in transmission mode every 7 s during deformation and analyzed stress-sensitive vibrational modes by Gaussian peak fitting to extract peak positions and track load-induced shifts [9].

Results and Discussions

We validated the BFDGE–DETDA and DGEBA–DETA (Figure 1) epoxy networks for structural and mechanical properties. Their densities, elastic moduli, stress–strain behavior, and viscoelastic relaxation profiles show good agreement with experimental and prior simulation data [52, 53, 54, 55, 56, 12, 13, 57, 58]. Full validation details are provided in the Supplementary Information (Section S1).

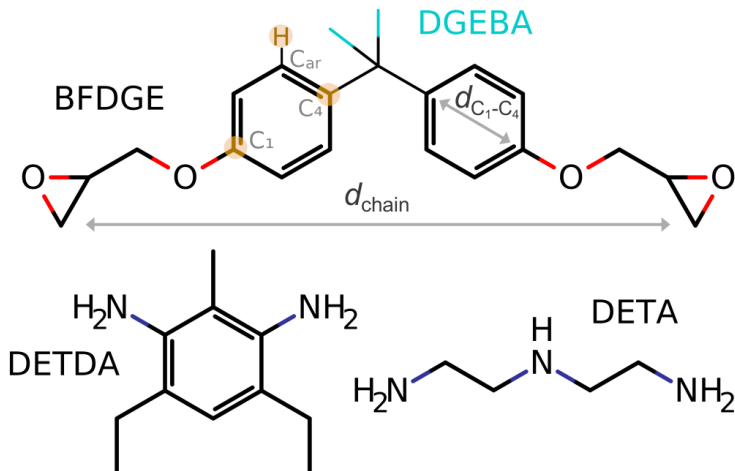


Figure 1: Chemical structures of the epoxy networks studied. The monomers BFDGE and DGEBA are shown, with additional methyl groups in DGEBA highlighted in cyan. The structures of the hardeners DETDA and DETA are also displayed. Atoms relevant to aromatic vibrational modes – specifically the C_1 and C_4 positions on the aromatic rings and one C_{ar} –H group – are highlighted in orange.

From the equilibrated structures obtained after constant-strain relaxation, we sampled atomic velocities using both the classical OPLS-AA force field [23] and the ML potential MACE-OFF23 [48]. Based on the resulting trajectories and RESP-fitted atomic charges, we computed the charge-weighted velocity autocorrelation function ($C_{JJ}(\tau)$; Equation 4) and obtained vibrational spectra by Fourier transformation.

We observed significant differences in the wavenumber region associated with *para*-phenylene vibrations (Figure 2). The carbon atoms of the *para*-phenylene unit respon-

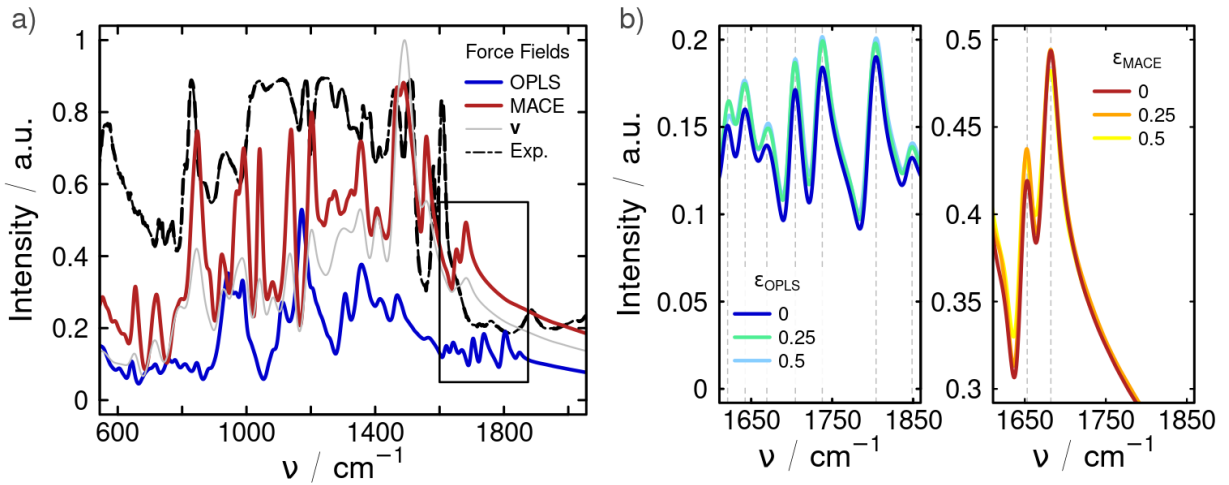


Figure 2: Comparison of vibrational spectra derived from different force fields. a) The 600–1800 cm^{-1} region highlights differences between the OPLS-AA and MACE-OFF23 potentials. Gray curves show spectra from the classical VACF (Equation 2), illustrating the lower peak resolution of this approach. Colored curves show spectra from the charge-weighted VACF_q, with sharper, more assignable peaks. The black dashed line represents the experimental spectrum, which is slightly redshifted due to the macroscopic electrostatic environment. b) Close-up of the wavenumber region where *para*-phenylene vibrations are expected.

sible for these modes – highlighted in Figure 1 – correspond to features also detected in experimental IR spectra [9]. In the 1600–1800 cm^{-1} region, where aromatic vibrations are expected, the OPLS-AA model produced multiple peaks that could not be clearly assigned and showed no systematic strain dependence. This behavior reflects the harmonic spring parameters used for aromatic bonds, which generate coupled modes and diffuse spectral features. In contrast, the MACE-OFF23-derived spectrum showed two well-resolved peaks: one near 1650 cm^{-1} , assigned to the symmetric stretch of the *para*-phenylene group, and another around 1680 cm^{-1} , associated with aromatic vibrations in the DETDA moiety of the polymer network. These features agree with experimental and quantum data [9], confirming the improved spectral fidelity of the MACE-OFF23 model.

The strain-dependent peak positions further illustrate these differences (Table 1). As expected from its harmonic nature, OPLS-AA yields essentially unchanged frequencies with increasing strain. By contrast, MACE-OFF23 predicts a clear and systematic redshift. This behavior reflects anharmonic bond softening under load, which harmonic force fields cannot reproduce. Because MACE-OFF23 is trained on quantum-level data, it captures the curvature of the potential energy surface and thus the correct strain-induced frequency shifts. The contrast highlights the inadequacy of harmonic potentials for vibra-

Table 1: Vibrational wavenumbers derived from the charge-weighted velocity autocorrelation function (VACF_q) for the OPLS-AA and MACE-OFF23 force fields at different strain levels (ϵ) in the BFDGE-DETDA system. The indices (1–7) correspond to the peak positions identified in Figure 2b.

ϵ	$\nu_{\text{OPLS}} / \text{cm}^{-1}$						
	ν_1	ν_2	ν_3	ν_4	ν_5	ν_6	ν_7
0	1621	1642.6	1669.4	1704.6	1737.8	1804.2	1848.6
0.25	1622.6	1642.2	1671	1704.2	1738.2	1803.4	1848.6
0.5	1623	1641.8	1671	1704.6	1737.8	1804.2	1849
$\nu_{\text{MACE}} / \text{cm}^{-1}$							
0	1653	1682.2	—	—	—	—	—
0.25	1652.6	1681.8	—	—	—	—	—
0.5	1651.8	1681.4	—	—	—	—	—

tional properties, while demonstrating that ML potentials provide significantly improved fidelity. This is particularly evident in the redshift of the C₁–C₄ mode of the aromatic *para*-phenylene ring, which emerges as a sensitive spectral fingerprint of local strain.

To enhance the accuracy of the vibrational spectra and facilitate more precise assignments, we isolated the velocities of the C₁–C₄ and C_{ar}–H atoms. Including all atomic velocities introduces motion from atoms bonded to the aromatic ring – such as bridging oxygens and adjacent carbons – that couple with ring vibrations and obscure intrinsic IR modes. These contributions primarily broaden and shift peaks without adding information.

By isolating the aromatic contributions through evaluation of the charge-weighted velocity autocorrelation function using only the velocities of the aromatic atoms (Figure 3), we obtained spectra that selectively emphasize aromatic vibrational modes. The analysis focused on characteristic features: the C₁–C₄ stretching modes (shown in red), comprising a symmetric stretch near 1650 cm^{−1} and an asymmetric stretch around 1550 cm^{−1}, and the C_{ar}–H bending modes (shown in blue), including an out-of-plane (oop) vibration at approximately 850 cm^{−1} and an in-plane (ip) vibration near 990 cm^{−1} [59]. This decomposition sharpened peak assignment and clarified the molecular origins of the aromatic features within the epoxy network.

Using this method, we extracted vibrational peaks for both epoxy systems, sampled with the MACE-OFF23 potential, under uniaxial deformation in all three spatial directions

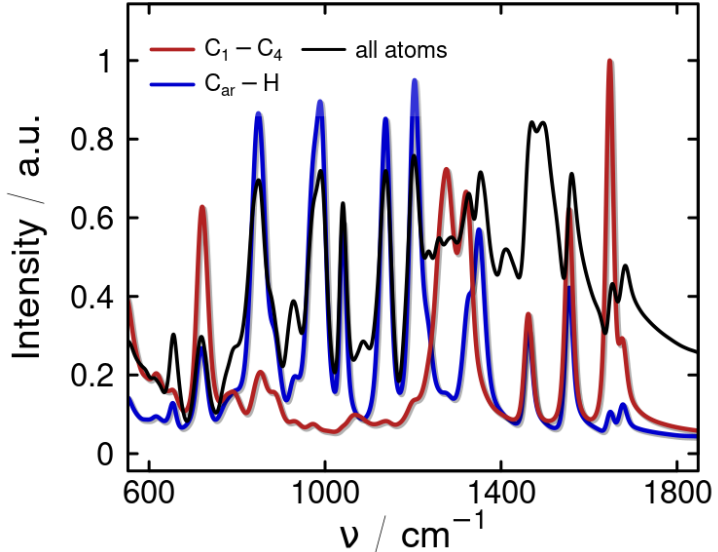


Figure 3: Vibrational spectrum showing the contributions of specific atomic groups to the total signal. The spectrum computed from all atomic velocities is shown in black. The red curve corresponds to the isolated C_1 – C_4 atoms of the aromatic ring, while the blue curve represents the hydrogen atoms attached to the *para*-phenylene group.

(x, y, z) (Figure 4). For each strain level ($\epsilon = 0, 0.03, 0.05, 0.125, 0.25, 0.375, 0.5$), spectra were computed independently for deformation along each axis, and the resulting peak positions were averaged. We included the standard deviation across directions as an error bar, capturing the mechanical anisotropy of the networks in their vibrational response.

As shown in Figure 4 a) and b), we observed a consistent redshift in the *para*-phenylene stretch vibrations of both epoxy systems with increasing strain. The magnitude of this shift agrees with creep experiments, which report $\frac{d\nu_{\text{exp}}}{d\epsilon} = -1.5, \text{cm}^{-1}$ [9]. At zero strain, the BFDGE–DETDA system showed a slightly higher frequency for the symmetric stretch vibration compared to DGEBA–DETA, whereas the opposite trend was observed for the asymmetric stretch, where DGEBA–DETA exhibited a higher-frequency peak. This difference likely arises from the methyl substituents on the DGEBA aromatic rings (see Figure 1, highlighted in cyan), which modify the local environment of the symmetric and asymmetric modes in opposite ways. Despite these differences in absolute wavenumbers, the overall redshift behavior under strain was consistent across both systems, reinforcing the predictive reliability of the simulations.

In order to directly validate the simulated strain-dependent spectral shifts, we performed *in-situ* infrared measurements during uniaxial tensile loading on 30 μm epoxy films.

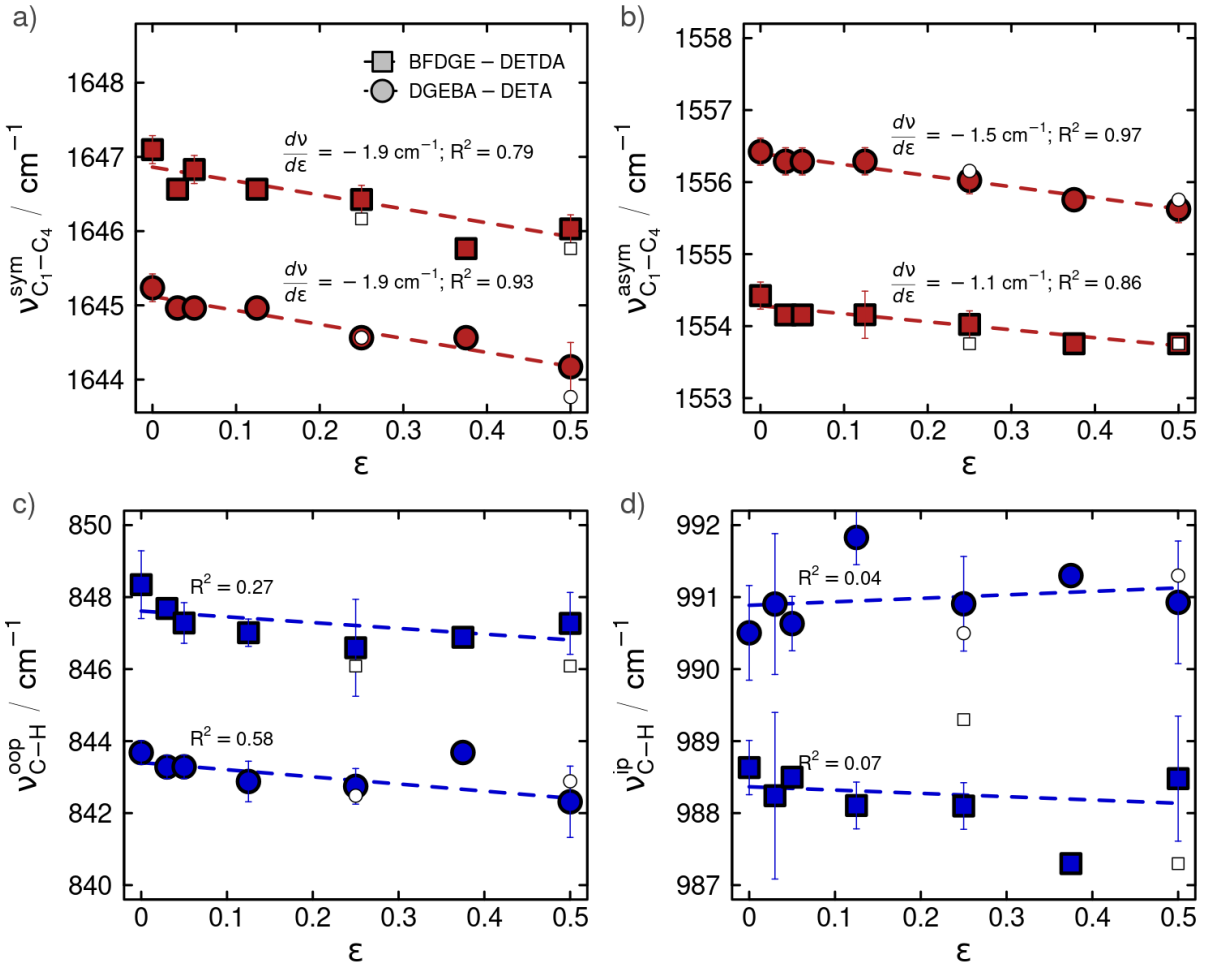


Figure 4: Vibrational peak shifts of the *para*-phenylene group under increasing strain for both epoxy systems, with linear fits applied to the extracted data. Error bars indicate the standard deviation across deformation along the x -, y -, and z -directions. White data points represent simulations conducted at a tenfold reduced strain rate. a) Symmetric stretch vibration: a linear redshift was observed in both systems, closely matching the experimentally reported value of -1.5 cm^{-1} [9], as reflected in the fitted slopes. b) Asymmetric stretch vibration: a similar redshift trend with increasing strain was observed, reinforcing the reproducibility of strain-dependent vibrational behavior in the simulations. c)/d) For both bending modes, no significant trend toward red- or blueshifting was detected across strain levels.

Six independent tensile tests were carried out at different strain rates ($\dot{\epsilon} = 0.2\text{--}1.0 \text{ mm min}^{-1}$). The mechanical response showed an average ultimate tensile strength of $58.6 \pm 5.2 \text{ MPa}$ and a elongation at break of 0.073 ± 0.017 . The peak positions at zero strain were located at 1608.3 cm^{-1} ($\nu_{\text{C}_1-\text{C}_4}^{\text{sym}}$), 1581.2 cm^{-1} ($\nu_{\text{C}_1-\text{C}_4}^{\text{asym}}$), and 830.9 cm^{-1} ($\nu_{\text{C}-\text{H}}^{\text{oop}}$). Linear regression of the peak shifts yielded average slopes of $-2.56 \pm 0.49 \text{ cm}^{-1}$ for the symmetric stretch, $-2.20 \pm 0.58 \text{ cm}^{-1}$ for the asymmetric stretch, and $-1.30 \pm 1.53 \text{ cm}^{-1}$ for the out-of-plane bending vibration. The latter mode shows only weak and inconsistent shifts. In the representative experiment shown in Figure 5, a small apparent blueshift is visible (slope

$+0.44 \text{ cm}^{-1}$), but this effect was absent in the majority of tests, confirming that bending vibrations of aromatic hydrogen atoms are far less sensitive to tensile deformation than the *para*-phenylene stretches in the backbones. Additionally, the corresponding redshifts of the symmetric and asymmetric stretching vibrations are in excellent agreement with the simulation data shown in Figure 4.

The mechanical properties, including ultimate tensile strength and elongation at break, showed no systematic dependence on strain rate. In contrast, the $\nu_{\text{C}_1-\text{C}_4}^{\text{sym}}$ and $\nu_{\text{C}_1-\text{C}_4}^{\text{asym}}$ stretching vibrations exhibited a tendency toward larger redshift slopes at slower strain rates, whereas the $\nu_{\text{C}-\text{H}}^{\text{oop}}$ bending vibration showed no reproducible trend. The variability across experiments attributed to sample-to-sample differences arising from the manual preparation of thin films, such as slight variations in thickness or the presence of micro-defects. The data shown in Figure 5 represent a typical test at $\dot{\epsilon} = 0.5 \text{ mm/min}$, while additional results at different strain rates and the corresponding strain rate dependency are provided in Supplementary Section S3.

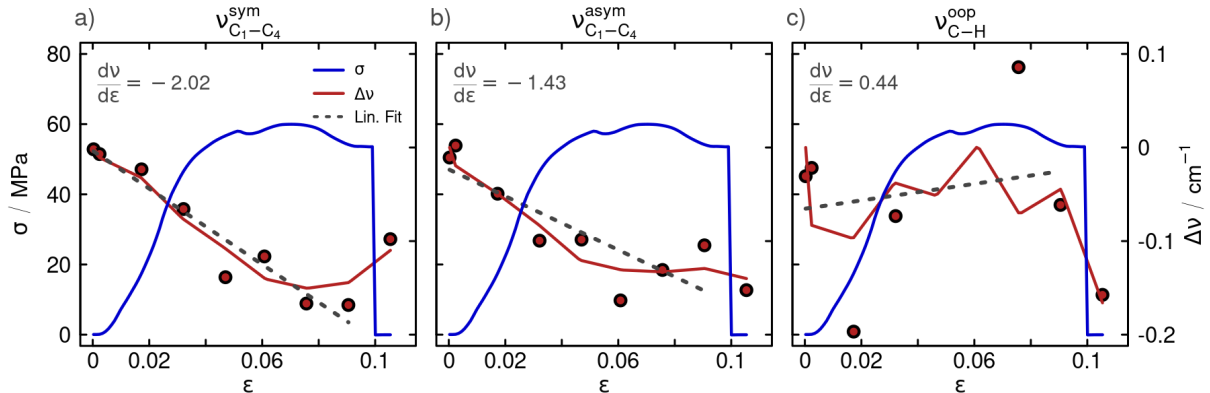


Figure 5: Experimentally measured strain-dependent peak shifts obtained from *in-situ* IR tensile testing of epoxy films. a) $\nu_{\text{C}_1-\text{C}_4}^{\text{sym}}$ stretch, b) $\nu_{\text{C}_1-\text{C}_4}^{\text{asym}}$ stretch, and c) $\nu_{\text{C}-\text{H}}^{\text{oop}}$ bending vibration. Blue curves represent the stress-strain response (σ), red curves the peak shift ($\Delta\nu$), and black circles the fitted peak positions. Dashed gray lines indicate linear fits with corresponding slopes ($d\nu/d\epsilon$).

To extend the vibrational analysis, we investigated the bending modes of the hydrogen atoms attached to the aromatic ring, as shown in Figure 4 c) and d). According to the findings of Mittelhaus *et al.* [9], stretching of the *para*-phenylene group leads to a blueshift in these bending vibrations. In the present study, we analyzed the bending modes analogously to the stretches, but the peak positions were highly scattered, remaining nearly constant or showing only slight shifts to lower wavenumbers. Because the coefficients of

determination (R^2) were low, we could not confirm a consistent blueshift. This discrepancy may be attributed to limitations of the MACE-OFF23 potential. In particular, polarization changes associated with aromatic deformation were likely absent from the training data. Moreover, the employed ML architecture lacks explicit atomic charges, which may prevent it from capturing subtle electronic effects such as those governing shifts in polar modes.

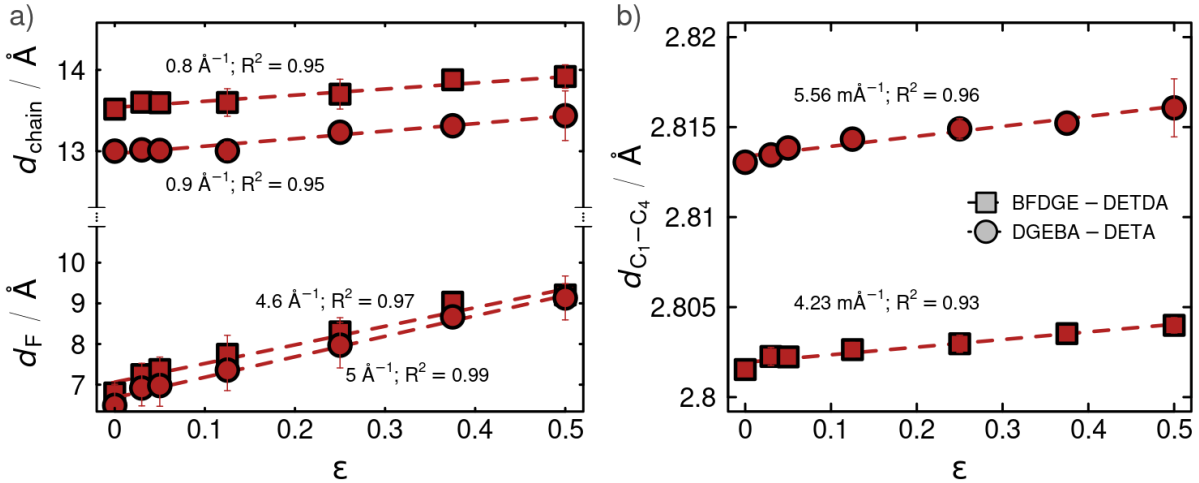


Figure 6: a) Evolution of the inter-chain distance d_{chain} and the aligned component of the distance vector in the direction of tension, d_F , as a function of strain for both epoxy systems. b) Corresponding changes in the aromatic ring spacing $d_{C_1-C_4}$ with strain. The slope values indicate the rate of change with applied strain.

To elucidate the origin of the redshift observed in the stretching modes, we analyzed the molecular configuration of the resin molecules – specifically their orientation and extension – following the methodology outlined in a previous study [9]. The elongation of the polymer backbone was quantified by the inter-terminal carbon distance, d_{chain} , for each resin molecule. The component of this distance aligned with the direction of applied force and strain, denoted as d_F , was also evaluated. As shown in Figure 6 a), both d_{chain} and d_F increased approximately linearly with strain, indicating that the polymer network accommodated deformation through a combination of segmental extension and alignment [9]. The quantities d_{chain} and $d_{C_1-C_4}$, used to characterize these structural changes, are schematically marked in Figure 1. Here, d_F denotes the component of the chain vector aligned with the applied strain direction (e.g. the x -axis for ϵ_x): $d_{\text{chain}} = \left\| \begin{pmatrix} d_F & y & z \end{pmatrix} \right\|$

Stronger chain alignment was observed in the DGEBA–DETA system than in BFDGE–DETDA, as reflected by the steeper slope of d_{chain} and d_F in response to strain. This structural adaptation induced elongation of the *para*-phenylene group, quantified by the distance between C₁ and C₄ atoms, $d_{\text{C}_1\text{--C}_4}$, which correlates with the redshift of its vibrational modes in accordance with Badger’s rule [60]. The linear relationship observed in Figure 6 b) confirms that strain-induced molecular elongation of the aromatic ring directly contributes to the frequency shifts in the vibrational spectra. This trend highlights the increased stretching of *para*-phenylene units in the DGEBA–DETA system, consistent with its stronger overall alignment behavior.

Although both epoxy systems exhibited broadly similar trends, subtle but meaningful differences emerged. In DGEBA–DETA, chain alignment was approximately 20 % more pronounced than in BFDGE–DETDA, as indicated by the slope of d_F . This stronger alignment was accompanied by an increase of $d_{\text{C}_1\text{--C}_4}$. However, the corresponding redshift of the *para*-phenylene stretching modes did not scale proportionally. This discrepancy suggests that the spectral response is governed not only by geometric elongation but also by local network flexibility, anharmonic coupling, and vibrational mode mixing.

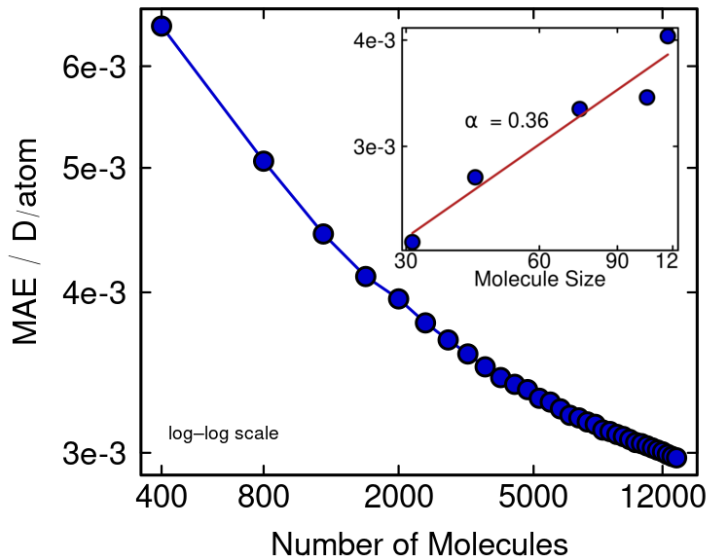


Figure 7: Learning curve of the SAGPR dipole model. The inset shows that the per-atom error increases super-linearly with molecule size, following $\varepsilon/n \sim n^\alpha$ with $\alpha \approx 1/3$.

Figure 7 shows the learning curve for the μ -EPOXY model for molecular dipole moments. Using 80 % of the training set, an SAGPR model was built that gives an error of 0.00297323 D/atom on an independent validation set, or $\sim 5\%$ of the intrinsic deviation

in the training set. This error is somewhat larger than that reported for recent models of water polarization ($\sim 1\%$) [36, 38], reflecting the greater structural complexity and size dispersity of the epoxy fragments studied here. In the inset of Figure 7 we show the prediction error as a function of molecular size in the validation set. The error in predicting dipole moment per atom shows a weak size dependence, increasing approximately as $\varepsilon/n \sim n^\alpha$ with $\alpha \approx 1/3$, where n is the number of atoms and ε the prediction error. This trend suggests that care should be taken when applying the model to arbitrarily large systems. Its most meaningful test of extrapolative ability, however, lies in the present application to epoxy networks.

To connect the bulk-epoxy network analysis with the molecular-level SAGPR study, we quantified the modification of key internal distances in the DBD fragment under controlled elongation. As shown in Figure 8, the molecular extension Δd_{mol} was accompanied by a concomitant increase of the aromatic ring span $d_{\text{C}_1\text{--C}_4}$, corresponding to the same geometric lever identified in the networks (Figure 6b). At the largest imposed elongation ($\Delta d_{\text{mol}} = 10 \text{ \AA}$), we observed a drop in inter-fragment distance, reflecting dissociation of the initially formed epoxy linkage. This behavior indicates that substantial tensile load is borne by the *para*-phenylene unit prior to bond rupture and shows that the MACE-OFF23 potential captures bond breaking on the underlying quantum-mechanical surface. In contrast, fixed-topology classical force fields with harmonic bond terms cannot represent dissociation [16].

The vibrational response of the DBD fragment was first analyzed by comparing power spectra derived from atomic velocities with those obtained from μ -EPOXY-predicted dipoles. As shown in Figure 9, the velocity-based spectrum (gray) exhibits a large number of vibrational features, many of which are not infrared-active. In contrast, the dipole-based spectrum (black) highlights only the IR-active modes, thereby providing a more direct comparison with experiments.

To assign specific peaks within the spectra, we applied targeted autocorrelation function–fast Fourier transform (ACF–FFT). For the symmetric stretching vibration of the *para*-phenylene group, we sampled the $\text{C}_1\text{--C}_4$ distance and computed its power spectrum (red curve in Fig. 9). Analogously, we isolated the out-of-plane bending motion of the

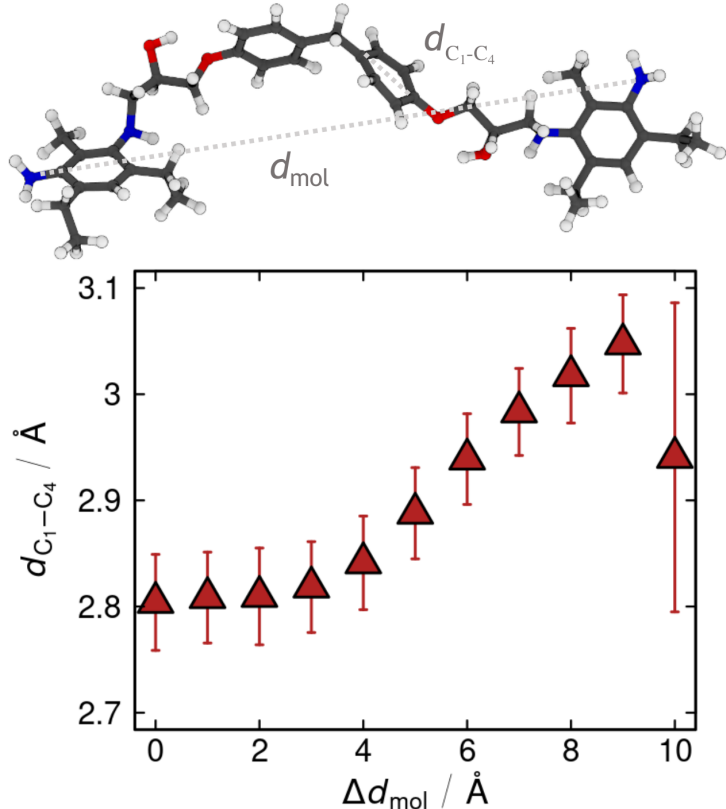


Figure 8: DBD fragment under controlled elongation. The aromatic span $d_{C_1-C_4}$ increases with Δd_{mol} , then drops at $\Delta d_{\text{mol}} = 10 \text{\AA}$ due to epoxy bond dissociation. Error bars indicate variability across configurations at each elongation.

aromatic hydrogens by calculating fluctuations of the corresponding distance coordinate and transforming them into the frequency domain (blue curve in Fig. 9). This approach allowed us to unambiguously assign peaks to distinct vibrational modes, providing a direct structural interpretation of the spectral features.

Peak positions were subsequently extracted from the spectra at each imposed molecular elongation. As shown in Figure 10, the symmetric stretch of the *para*-phenylene group initially appeared near 1670 cm^{-1} (red), while the out-of-plane bending vibration of the aromatic hydrogens was located around 830 cm^{-1} (blue). Tracking these frequencies as a function of Δd_{mol} revealed a pronounced redshift of the stretching mode, in agreement with the bulk-network analysis of the power spectra. The fitted trend line confirms that the redshift coincides with the increase of the $d_{C_1-C_4}$ distance, thereby establishing a direct link between molecular elongation and redshifting of the aromatic stretch vibration $\nu_{C_1-C_4}$.

Importantly, the out-of-plane bending vibration was also captured in the dipole-derived spectra, but not in the velocity-based spectra, underscoring the advantage of dipole auto-

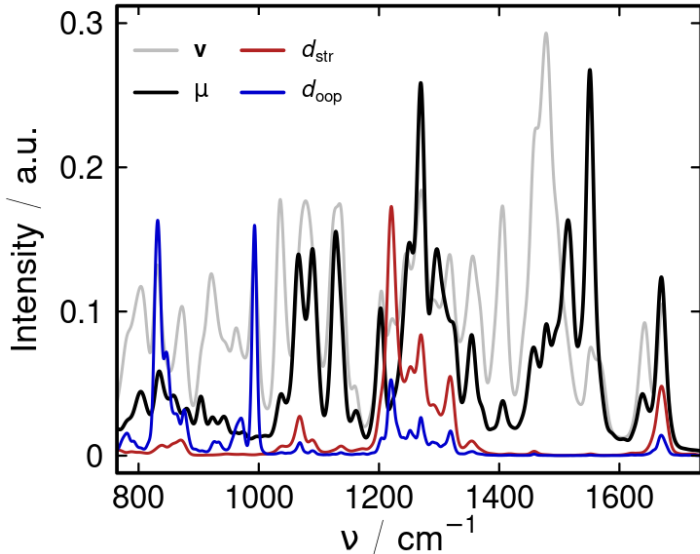


Figure 9: Comparison of vibrational spectra of the DBD fragment obtained from different autocorrelation functions. The velocity-based spectrum (gray) exhibits many features not IR-active. In contrast, the dipole-based spectrum (black) highlights only IR-active modes. Targeted ACF–FFT workflows were applied to specific internal coordinates: C_1 – C_4 distance (red) for the symmetric aromatic stretch (str), and the out-of-plane (oop) motion of aromatic hydrogens (blue) for bending vibrations.

correlation functions for detecting IR-active modes. The identification of both stretching and bending responses shows that the dipole-enhanced workflow captures a broader range of vibrational behavior under strain, strengthening its predictive power.

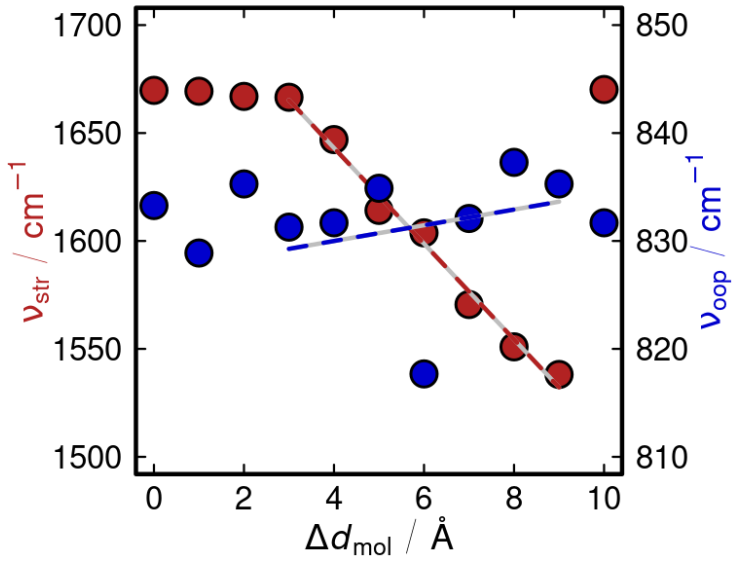


Figure 10: Tracked peak positions of the symmetric stretch vibration of the *para*-phenylene group (red, left axis) and the out-of-plane bending vibration of aromatic hydrogens (blue, right axis) as a function of molecular elongation Δd_{mol} . Linear fits highlight the redshift of the stretching mode with increasing Δd_{mol} and the weak blueshift of the bending mode.

The results show that the redshift of the symmetric stretch is substantially stronger than the weak blueshift of the out-of-plane bending mode. This disparity is explained by the fact that the redshift directly reflects the elongation of the C₁–C₄ distance [60], whereas the blueshift is only a secondary consequence of aromatic ring deformation, as discussed by Mittelhaus *et al.* [9].

An additional point of significance is the demonstrated generalization capability of the μ -EPOXY model. Although the training data did not include structures with C₁–C₄ distances exceeding 3.0 Å, the model nevertheless reproduced the expected frequency trend under elongation with high fidelity. Thus, the model not only interpolates within its training domain but also extrapolates in a physically meaningful way.

Crucially, the consistent redshift observed in both epoxy networks (BFDGE–DETDA and DGEBA–DETA) and in the strained DBD fragment demonstrates that the *para*-phenylene stretches provide robust spectral markers of mechanical strain. The agreement between MACE-based bulk spectra and SAGPR–derived fragment spectra validates the fidelity of the ML descriptions and indicates that vibrational observables can be exploited to localize stress in aromatic epoxy networks. Due to their sensitivity to molecular alignment and C₁–C₄ elongation, these modes are well suited for non-destructive strain mapping in polymer composites, providing a foundation for computationally guided diagnostics and structural-health monitoring, contingent on appropriate peak–strain calibration and accounting for network anisotropy (cf. Figure 4).

Conclusions

We developed a computational framework to predict strain-dependent vibrational responses in crosslinked epoxy networks, providing spectroscopic access to local mechanical deformation. By comparing classical (OPLS-AA) and machine-learned (MACE-OFF23) force fields, we showed that only the ML model captures the anharmonic bond softening responsible for redshifts in aromatic stretching modes under load. These shifts, observed across two chemically distinct epoxy systems, are in qualitative agreement with earlier *in-situ* IR measurements performed under different loading conditions [9] and in quantitative

agreement with the *in-situ* tensile data presented here, and they correlate with molecular-scale elongation and orientation, in accordance with Badger’s rule. The demonstrated agreement between simulation and experiment supports the use of vibrational fingerprints as reliable, predictive markers of mechanical state in polymer networks.

Through atom-specific spectral decomposition and the use of charge-weighted velocity autocorrelations, vibrational signatures were linked to backbone alignment and *para*-phenylene ring extension. These features serve as molecular-level indicators of mechanical strain and can be accessed through infrared spectroscopy. Although polarization effects were not fully resolved – leading to limited accuracy in bending modes – the MACE model provided chemically realistic and spectrally consistent results, highlighting the ability of ML force fields to capture deformation-sensitive vibrational behavior in polymers.

Complementary dipole modeling further demonstrated that IR-active features, including the out-of-plane bending of aromatic hydrogens, can be resolved with higher fidelity than velocity-based spectra alone. The agreement between bulk-network spectra (from MACE) and fragment-level dipole spectra confirms that combining force-field and dipole learning approaches provides a consistent description across scales. The μ -EPOXY model also reproduced strain-induced shifts even outside its training domain, demonstrating its potential to predict vibrational observables under deformation and its meaningful extrapolation capability.

These insights directly extend to composite applications, where epoxy matrices govern reliability under load. Linking vibrational fingerprints to mechanical strain provides a pathway for non-destructive diagnostics and lifetime assessment in structural materials.

This work represents the first demonstration of MACE-OFF23 for epoxy networks, establishing its suitability for complex crosslinked systems beyond the small molecules and condensed phases for which it was originally trained. Our results show that ML potentials offer chemically realistic and computationally tractable access to vibrational fingerprints of mechanical state in thermoset polymers. Coupling vibrational spectroscopy with ML force fields thus provides a viable route to non-destructive diagnostics, stress mapping, and failure prediction in structural polymers.

Future extensions to other thermoset systems, supported by extensive quantum-mechanical training data, are expected to enable unified architectures that simultaneously predict interatomic forces and electronic observables. Such polarization-aware neural network models [30] would deliver an all-in-one description of mechanical and spectroscopic responses under deformation, enhancing transferability and predictive power.

Acknowledgments

This research received funding from Grant No. 525597740 provided by the Deutsche Forschungsgemeinschaft (DFG, German Research Foundation).

Competing interests

The authors have no competing interests to declare.

Author contributions

Conceptualization: JK, RM Methodology: JK, DW, JM, BF, RM Investigation: JK, DW, JM Visualization: JK Supervision: RM, BF Writing-original draft: JK Writing-review & editing: JK, DW, JM, BF, RM

Data availability

The data supporting this study are available from the corresponding author upon reasonable request; due to their multi-terabyte size, data sharing will be coordinated accordingly.

Supplementary Materials

The supplementary information includes: Supplementary Text, Figures S1–S5, Tables S1 and S2.

References

- [1] S. Mukherjee and A. Gowen, “A review of recent trends in polymer characterization using non-destructive vibrational spectroscopic modalities and chemical imaging,” *Analytica Chimica Acta*, vol. 895, p. 12–34, Oct. 2015.
- [2] F.-L. Jin, X. Li, and S.-J. Park, “Synthesis and application of epoxy resins: A review,” *Journal of Industrial and Engineering Chemistry*, vol. 29, p. 1–11, Sept. 2015.
- [3] P. K. Balguri, D. H. Samuel, and U. Thumu, “A review on mechanical properties of epoxy nanocomposites,” *Materials Today: Proceedings*, vol. 44, p. 346–355, 2021.
- [4] F. A. Gilabert, D. Garoz, R. Sevenois, S. Spronk, A. Rezaei, W. V. Paepegem, and ESCM, “Composite micro-scale model accounting for debonding, strain-rate dependence and damage under impact using an explicit finite element solver,” *17th European Conference on Composite Materials*, pp. 1–8, 2016.
- [5] T. J. Vaughan and C. T. McCarthy, “Micromechanical modelling of the transverse damage behaviour in fibre reinforced composites,” *Composites Science and Technology*, vol. 71, no. 3, pp. 388–396, 2011.
- [6] W. Tan, F. Naya, L. Yang, T. Chang, B. G. Falzon, L. Zhan, J. M. Molina-Aldareguía, C. González, and J. LLorca, “The role of interfacial properties on the intralaminar and interlaminar damage behaviour of unidirectional composite laminates: Experimental characterization and multiscale modelling,” *Composites Part B: Engineering*, vol. 138, pp. 206–221, 2018.
- [7] O. Verschatse, L. Daelemans, W. Van Paepegem, and K. De Clerck, “In-situ observations of microscale ductility in a quasi-brittle bulk scale epoxy,” *Polymers*, vol. 12, p. 2581, Nov. 2020.
- [8] J. Mittelhaus, P. Röttger, E. Schill, J. Jacobs, and B. Fiedler, “Investigation of the ductile deformation potential of microscale epoxy materials,” *Polymer Testing*, vol. 128, p. 108217, Nov. 2023.

[9] J. Mittelhaus, J. Konrad, J. Jacobs, P. Röttger, R. Meißner, and B. Fiedler, “Load-induced shear band formation in microscale epoxy materials,” *Journal of Polymer Science*, vol. 63, pp. 2174–2186, Mar. 2025.

[10] V. Varshney, S. S. Patnaik, A. K. Roy, and B. L. Farmer, “A molecular dynamics study of epoxy-based networks: Cross-linking procedure and prediction of molecular and material properties,” *Macromolecules*, vol. 41, p. 6837–6842, Aug. 2008.

[11] T. Okabe, Y. Oya, K. Tanabe, G. Kikugawa, and K. Yoshioka, “Molecular dynamics simulation of crosslinked epoxy resins: Curing and mechanical properties,” *European Polymer Journal*, vol. 80, p. 78–88, July 2016.

[12] R. H. Meißner, J. Konrad, B. Boll, B. Fiedler, and D. Zahn, “Molecular simulation of thermosetting polymer hardening: Reactive events enabled by controlled topology transfer,” *Macromolecules*, vol. 53, p. 9698–9705, Nov. 2020.

[13] J. Konrad, R. H. Meißner, E. Bitzek, and D. Zahn, “A molecular simulation approach to bond reorganization in epoxy resins: From curing to deformation and fracture,” *ACS Polymers Au*, vol. 1, p. 165–174, Aug. 2021.

[14] C. Zhu, M. Liu, N. Wei, and J. Zhao, “Molecular dynamics study on mechanical properties of helical graphenes/epoxy nanocomposites,” *Computational Materials Science*, vol. 209, p. 111408, June 2022.

[15] D. Esse, G. Sick, F. Henning, B. Fiedler, and W. V. Liebig, “Non-destructive assessment of strain and mechanical fatigue in neat and glass fibre-reinforced epoxy via nir spectroscopy,” *Polymer Testing*, vol. 151, p. 108960, Oct. 2025.

[16] A. R. Leach, *Molecular Modelling - Principles and Applications*. Amsterdam: Pearson Education, 2001.

[17] F. Jensen, *Introduction to Computational Chemistry*. New York: John Wiley & Sons, 2016.

[18] A. Doblies, C. Feiler, T. Würger, E. Schill, R. H. Meißner, and B. Fiedler, “Mechanical degradation estimation of thermosets by peak shift assessment: General approach using infrared spectroscopy,” *Polymer*, vol. 221, p. 123585, Apr. 2021.

[19] I. Dabo, A. Wieckowski, and N. Marzari, “Vibrational recognition of adsorption sites for co on platinum and platinum-ruthenium surfaces,” *Journal of the American Chemical Society*, vol. 129, p. 11045–11052, Aug. 2007.

[20] M. Praprotnik, D. Janežič, and J. Mavri, “Temperature dependence of water vibrational spectrum: A molecular dynamics simulation study,” *The Journal of Physical Chemistry A*, vol. 108, p. 11056–11062, Nov. 2004.

[21] M. Thomas, M. Brehm, R. Fligg, P. Vöhringer, and B. Kirchner, “Computing vibrational spectra from ab initio molecular dynamics,” *Physical Chemistry Chemical Physics*, vol. 15, no. 18, p. 6608, 2013.

[22] Y. Zhang, Y. Wang, X. Xu, Z. Chen, and Y. Yang, “Vibrational spectra of highly anharmonic water clusters: Molecular dynamics and harmonic analysis revisited with constrained nuclear-electronic orbital methods,” *Journal of Chemical Theory and Computation*, vol. 19, p. 9358–9368, Dec. 2023.

[23] W. L. Jorgensen, D. S. Maxwell, and J. Tirado-Rives, “Development and testing of the opls all-atom force field on conformational energetics and properties of organic liquids,” *Journal of the American Chemical Society*, vol. 118, p. 11225–11236, Nov. 1996.

[24] M. Karplus and J. A. McCammon, “Molecular dynamics simulations of biomolecules,” *Nature Structural Biology*, vol. 9, p. 646–652, Sept. 2002.

[25] A. P. Bartók, M. C. Payne, R. Kondor, and G. Csányi, “Gaussian approximation potentials: The accuracy of quantum mechanics, without the electrons,” *Physical Review Letters*, vol. 104, Apr. 2010.

[26] J. Behler, “Perspective: Machine learning potentials for atomistic simulations,” *The Journal of Chemical Physics*, vol. 145, Nov. 2016.

[27] C. Schran, K. Brezina, and O. Marsalek, “Committee neural network potentials control generalization errors and enable active learning,” *The Journal of Chemical Physics*, vol. 153, Sept. 2020.

[28] O. T. Unke, S. Chmiela, H. E. Sauceda, M. Gastegger, I. Poltavsky, K. T. Schütt, A. Tkatchenko, and K.-R. Müller, “Machine learning force fields,” *Chemical Reviews*, vol. 121, p. 10142–10186, Mar. 2021.

[29] S. Batzner, A. Musaelian, L. Sun, M. Geiger, J. P. Mailoa, M. Kornbluth, N. Molinari, T. E. Smidt, and B. Kozinsky, “E(3)-equivariant graph neural networks for data-efficient and accurate interatomic potentials,” *Nature Communications*, vol. 13, May 2022.

[30] A. Musaelian, S. Batzner, A. Johansson, L. Sun, C. J. Owen, M. Kornbluth, and B. Kozinsky, “Learning local equivariant representations for large-scale atomistic dynamics,” *Nature Communications*, vol. 14, Feb. 2023.

[31] D. P. Kovács, J. H. Moore, N. J. Browning, I. Batatia, J. T. Horton, Y. Pu, V. Kapil, W. C. Witt, I.-B. Magdău, D. J. Cole, and G. Csányi, “Mace-off: Transferable short range machine learning force fields for organic molecules,” 2023.

[32] J. Deng, H. Niu, J. Hu, M. Chen, and L. Stixrude, “Melting of MgSiO₃ determined by machine learning potentials,” *Physical Review B*, vol. 107, Feb. 2023.

[33] Z. Yu and N. E. Jackson, “Exploring thermoset fracture with a quantum chemically accurate model of bond scission,” *Macromolecules*, vol. 57, p. 1414–1425, Feb. 2024.

[34] D. M. Wilkins, A. Grisafi, Y. Yang, K. U. Lao, R. A. DiStasio, and M. Ceriotti, “Accurate molecular polarizabilities with coupled cluster theory and machine learning,” *Proceedings of the National Academy of Sciences*, vol. 116, p. 3401–3406, Feb. 2019.

[35] M. Veit, D. M. Wilkins, Y. Yang, R. A. DiStasio, and M. Ceriotti, “Predicting molecular dipole moments by combining atomic partial charges and atomic dipoles,” *The Journal of Chemical Physics*, vol. 153, July 2020.

[36] V. Kapil, D. M. Wilkins, J. Lan, and M. Ceriotti, “Inexpensive modeling of quantum dynamics using path integral generalized langevin equation thermostats,” *The Journal of Chemical Physics*, vol. 152, Mar. 2020.

[37] P. Schienbein, “Spectroscopy from machine learning by accurately representing the atomic polar tensor,” *Journal of Chemical Theory and Computation*, vol. 19, p. 705–712, Jan. 2023.

[38] A. Jana, S. Shepherd, Y. Litman, and D. M. Wilkins, “Learning electronic polarizations in aqueous systems,” *Journal of Chemical Information and Modeling*, vol. 64, p. 4426–4435, May 2024.

[39] A. Grisafi, D. M. Wilkins, G. Csányi, and M. Ceriotti, “Symmetry-adapted machine learning for tensorial properties of atomistic systems,” *Physical Review Letters*, vol. 120, Jan. 2018.

[40] J. Mittelhaus, J. Jacobs, S. Bhusare, N. Pournoori, M. Isakov, T. Salminen, H. Schmalz, G. Mohanty, E. Sarlin, and B. Fiedler, “Performing polarized raman and digital image correlation analysis to understand the increased ductility of microscale epoxy materials,” *Journal of Polymer Science*, vol. 63, p. 2091–2101, Mar. 2025.

[41] D. Weininger, “Smiles, a chemical language and information system. 1. introduction to methodology and encoding rules,” *Journal of Chemical Information and Computer Sciences*, vol. 28, p. 31–36, Feb. 1988.

[42] L. S. Dodda, I. Cabeza de Vaca, J. Tirado-Rives, and W. L. Jorgensen, “Ligpargen web server: an automatic opls-aa parameter generator for organic ligands,” *Nucleic Acids Research*, vol. 45, p. W331–W336, Apr. 2017.

[43] J. Konrad and R. Meißner, “Smart reaction templating: A graph-based method for automated molecular dynamics input generation,” *Journal of Chemical Information and Modeling*, vol. 65, p. 6038–6047, June 2025.

[44] A. P. Thompson, H. M. Aktulga, R. Berger, D. S. Bolintineanu, W. M. Brown, P. S. Crozier, P. J. in 't Veld, A. Kohlmeyer, S. G. Moore, T. D. Nguyen, R. Shan, M. J.

Stevens, J. Tranchida, C. Trott, and S. J. Plimpton, “Lammps - a flexible simulation tool for particle-based materials modeling at the atomic, meso, and continuum scales,” *Computer Physics Communications*, vol. 271, p. 108171, Feb. 2022.

[45] J. R. Gissinger, B. D. Jensen, and K. E. Wise, “Modeling chemical reactions in classical molecular dynamics simulations,” *Polymer*, vol. 128, p. 211–217, Oct. 2017.

[46] D. J. Evans and B. L. Holian, “The nose–hoover thermostat,” *The Journal of Chemical Physics*, vol. 83, p. 4069–4074, Oct. 1985.

[47] R. W. Hockney and J. W. Eastwood, *Computer simulation using particles*. Bristol: Hilger, 1988, 1988.

[48] I. Batatia, D. P. Kovács, G. N. C. Simm, C. Ortner, and G. Csányi, “Mace: Higher order equivariant message passing neural networks for fast and accurate force fields,” 2022.

[49] F. Neese, “Software update: The orca program system—version 6.0,” *Wiley Interdisciplinary Rev. Comput. Mol. Sci.*, vol. 15, no. 2, p. e70019, 2025.

[50] V. L. Deringer, A. P. Bartók, N. Bernstein, D. M. Wilkins, M. Ceriotti, and G. Csányi, “Gaussian process regression for materials and molecules,” *Chemical Reviews*, vol. 121, p. 10073–10141, Aug. 2021.

[51] C. E. Rasmussen and C. K. I. Williams, *Gaussian processes for machine learning*. Adaptive Computation and Machine Learning series, London, England: MIT Press, Nov. 2005.

[52] K. Tao, S. Yang, J. C. Grunlan, Y.-S. Kim, B. Dang, Y. Deng, R. L. Thomas, B. L. Wilson, and X. Wei, “Effects of carbon nanotube fillers on the curing processes of epoxy resin-based composites,” *Journal of Applied Polymer Science*, vol. 102, no. 6, pp. 5248–5254, 2006.

[53] H. Cai, P. Li, G. Sui, Y. Yu, G. Li, X. Yang, and S. Ryu, “Curing kinetics study of epoxy resin/flexible amine toughness systems by dynamic and isothermal DSC,” *Thermochimica Acta*, vol. 473, pp. 101–105, July 2008.

[54] J. D. Littell, C. R. Ruggeri, R. K. Goldberg, G. D. Roberts, W. A. Arnold, and W. K. Binienda, “Measurement of epoxy resin tension, compression, and shear stress–strain curves over a wide range of strain rates using small test specimens,” *Journal of Aerospace Engineering*, vol. 21, no. 3, pp. 162–173, 2008.

[55] Hexion, *EPICOTE Resin 862*, 01 2009.

[56] S. V. Kallivokas, A. P. Sgouros, and D. N. Theodorou, “Molecular dynamics simulations of EPON-862/DETDA epoxy networks: structure, topology, elastic constants, and local dynamics,” *Soft Matter*, vol. 15, no. 4, pp. 721–733, 2019.

[57] I. Delasoudas, S. V. Kallivokas, and V. Kostopoulos, “Fracture of epoxy networks using atomistic simulations,” *The Journal of Physical Chemistry B*, vol. 128, p. 7271–7279, July 2024.

[58] J. J. Winetroub, K. Kanhaiya, J. Kemppainen, P. J. in ‘t Veld, G. Sachdeva, R. Pandey, B. Damirchi, A. van Duin, G. M. Odegard, and H. Heinz, “Implementing reactivity in molecular dynamics simulations with harmonic force fields,” *Nature Communications*, vol. 15, Sept. 2024.

[59] A. Andrejeva, A. M. Gardner, W. D. Tuttle, and T. G. Wright, “Consistent assignment of the vibrations of symmetric and asymmetric para-disubstituted benzene molecules,” *Journal of Molecular Spectroscopy*, vol. 321, p. 28–49, Mar. 2016.

[60] R. M. Badger, “A relation between internuclear distances and bond force constants,” *The Journal of Chemical Physics*, vol. 2, no. 3, pp. 128–131, 1934.